AIAA AVIATION Forum
June 25-29, 2018, Atlanta, Georgia
2018 Flow Control Conference

10.2514/6.2018-3062

Design of Injection and Suction Ducts for Co-Flow Jet Airfoils with Embedded Micro-Compressors Actuator

Yan Ren * Gecheng Zha †
Dept. of Mechanical and Aerospace Engineering
University of Miami, Coral Gables, Florida 33124
E-mail: gzha@miami.edu

Abstract

This paper presents the designs of injection and suction ducts of co-flow jet (CFJ) flow control airfoils with embedded micro-compressor actuator in cruise condition. The duct cross section outlines are mathematically modeled as superellipse, which has a parameter η to control the outline shape. Several geometry parameters are taken into consideration during the design process, including the shape parameter η, the cross section area of the duct, the semi major axis and semi minor axis of the superellipse. The aerodynamic performance of the ducts are evaluated via numerical simulations, which employ 3D RANS solver with Spalart-Allmaras (S-A) turbulence model, 3th order WENO scheme for the inviscid fluxes, and 2nd order central differencing for the viscous terms. The ducts inlet and outlet shapes are predetermined according to the micro-compressor performance, and the associated boundary conditions are configured based on the 2D simulation results of CFJ airfoils and micro-compressors. The design goal is to eliminate flow separation, maximize the total pressure recovery, and obtain a more uniformly distributed mass flow at the injection duct outlet.

The simulation results show that the duct cross section area distribution along the stream wise direction is crucial to control the duct diffusion and flow separation. For the suction duct, the superellipse semi major axis is important to improve the total pressure recovery. For the injection duct, the center body geometry is critical due to the large swirl angle of the flow from the micro-compressor outlet. Moreover, the injection duct guiding vanes can provide a more uniformly distributed mass flow at the duct outlet. Our optimized suction duct presents 99% total pressure recovery. The optimized injection duct shows 95% total pressure recovery without guiding vanes, and shows 93.7% total pressure recovery with guiding vanes.

Nomenclature

SD	Suction duct
ID	Injection duct
AFC	Active Flow Control
CFJ	Co-Flow Jet
LE	Leading edge
TE	Trailing edge
$FASIP$	Flow-Acoustics-Structure Interaction Package
$RANS$	Reynolds-Averaged Navier-Stokes

* Postdoc Researcher, Ph.D., AIAA member
† Professor, ASME Fellow, AIAA associate Fellow

$ZNMF$	Zero-Net Mass Flux
η	Superellipse shape parameter
β	Deviation angle
P_{tr}	Total pressure ratio
M	Mach number
Γ	Gamma function
ρ	Density
V	Velocity
P_{01}	Total pressure at the inlet
P_{02}	Total pressure at the outlet
$\dot{m}$	Mass flow rate
$_\infty$	Subscript, stands for free stream
$_{cs}$	Subscript, stands for cross section
$_i$	Subscript, stands for inlet
$_o$	Subscript, stands for outlet

1 Introduction

In the past three decades, Active Flow Control (AFC) has attracted lots of interests as a means to enhance the performance of airfoil, which otherwise has appeared to be saturated based on conventional airfoil shape optimization. Among the many AFC techniques that have been actively studied, Co-Flow Jet (CFJ) airfoil is a zero-net mass-flux (ZNMF) flow control method recently developed by Zha et al. [1, 2, 3, 4, 5, 6, 7, 8, 9, 10, 11]. It is demonstrated to achieve radical lift augmentation, stall margin increase, drag reduction and moderate nose-down moment for stationary and pitching airfoils.

In the CFJ airfoil concept, an injection slot near the leading edge (LE) and a suction slot near the trailing edge (TE) on the airfoil suction surface are created. As shown in Fig. 1, a small amount of mass flow is withdrawn into the suction duct, pressurized and energized by a micro-compressor, and then injected near the LE tangentially to the main flow via an injection duct. The whole process does not add any mass flow to the system and hence is a ZNMF flow control. The flow inside the airfoil (in the suction and injection ducts) are essential to the overall CFJ airfoil performance. Any flow separations within the ducts will increase the energy expenditure.

The purpose of this paper is to conduct the design of injection and suction ducts in cruise condition. The suction duct is connected to the micro-compressor actuator inlet and the injection duct is connected to the micro-compressor outlet. In the current designs, the duct inlet and outlet sizes and locations are predetermined by the 2D CFJ airfoil designs, so are the associated boundary conditions. The boundary conditions of the micro-compressor are determined by the design of the micro-compressor that meets the CFJ airfoil mass flow and pressure ratio requirements. The injection duct inlet is directly connected to the outlet of the micro-compressor, which presents a ring shape outline and generates swirl flow. In order to remove flow separation, a center body connecting to the inner circle of the micro-compressor outlet is used to guild the flow.

The requirements of the duct design in this paper are that there is no flow separation and the pressure recovery is as high as possible. Moreover, a uniform distribution of the mass flow at the injection slot and micro-compressor inlet are desirable.

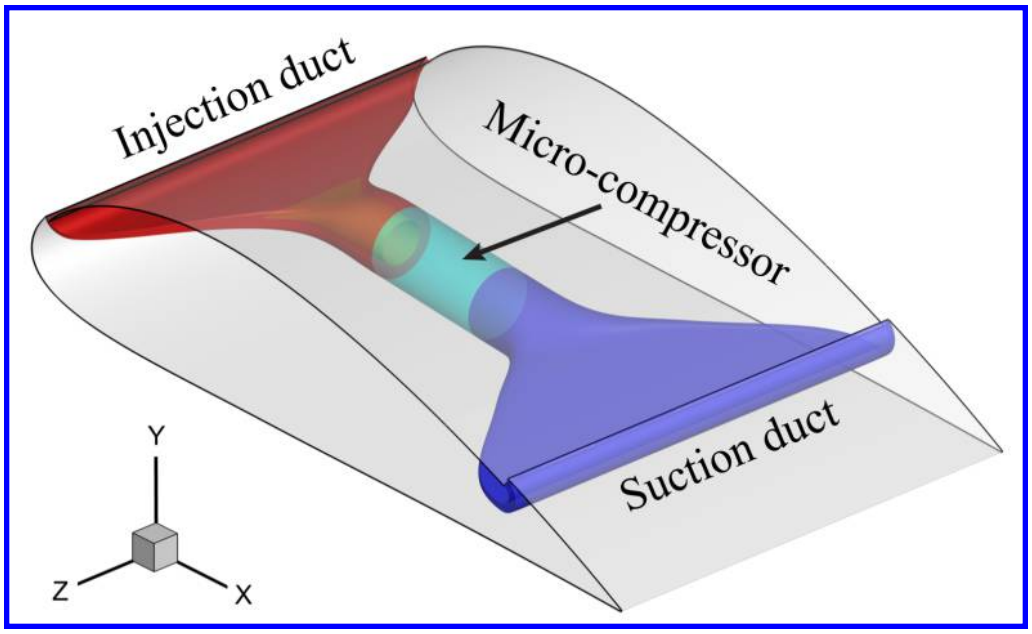

Figure 1: Schematic plot of a typical CFJ airfoil.

2 Methodology

2.1 Duct Geometry

As shown in Fig. 1, the duct inlet and outlet have different shapes. The inlet of suction duct and outlet of injection duct have rectangular shape, whereas the outlet of suction duct and inlet of injection duct have circular shape. The method of calculating circular-to-rectangular transition surfaces developed in [12] is adopted.

A circle, an ellipse, and a rectangle are all specific cases of superellipses. The locus of points which make up a superellipse is defined as:

$$(\frac{y}{a})^{\eta} + (\frac{z}{b})^{\eta} = 1 \tag{1}$$

where a and b are semi major and minor axis of the superellipse. η is shape parameter which controls the superellipse shape.

With a and b defined as continuous analytic functions of x (axis distance from the entrance), the transition surface is determined by iteratively computing $\eta(x)$ from Eq. (1). For practical applications, a rectangle ($\eta = \infty$) is accurately approximated with $\eta \geq 50$. In this paper, $\eta = 100$ is used to represent a rectangle.

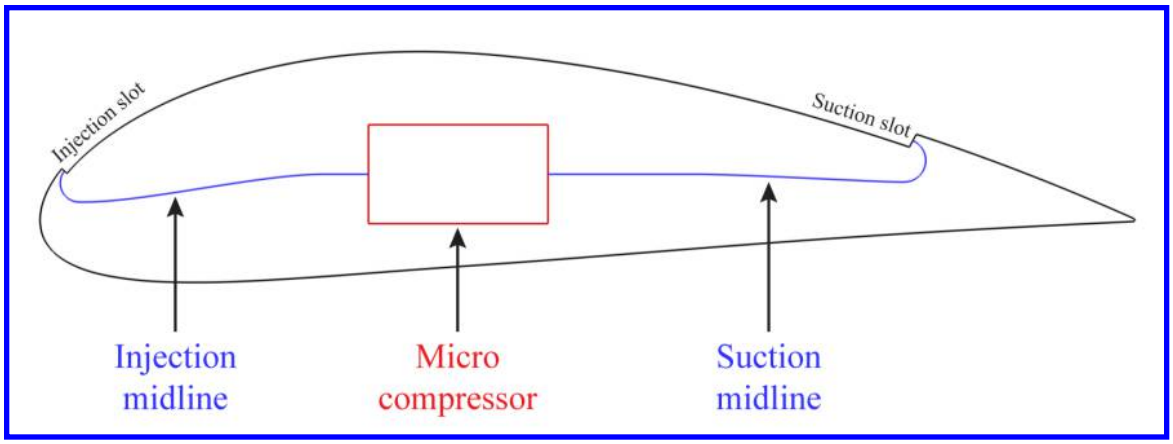

Figure 2: CFJ airfoil configuration in cruise condition. The airfoil used here is CFJ-NACA 6421.

As shown in Fig. 2, the CFJ airfoil injection and suction slot dimensions and locations are determined according to our previous published 2D design [13]. The injection and suction duct meanlines are determined based on the slot locations (blue curves in Fig. 2). We create superellipses along those duct meanlines, which pass through the superellipse geometric centers and locally perpendicular to the superellipses. The duct surfaces are formed by connecting those superellipses. Based on above mathematical model and geometry configuration, we successfully parameterize the problem, which is essential to the designs of the CFJ injection and suction ducts.

2.2 Total Pressure Recovery

The best way of evaluating performance of a given duct is to calculate the total pressure recovery, which is defined as follows:

$$P_{tr} = \frac{\oiint_{S_o} \rho \mathbf{V} P_{02} d\mathbf{A}}{\oiint_{S_i} \rho \mathbf{V} P_{01} d\mathbf{A}} \tag{2}$$

where S_o and S_i stand the cross section interface at the inlet and outlet, respectively. P_{02} and P_{01} are the total pressure evaluated at outlet and inlet. The total pressure recovery P_{tr} is basically the mass averaged total pressure ratio of outlet cross section and inlet cross section.

2.3 CFD Simulation Setup

The FASIP (Flow-Acoustics-Structure Interaction Package) CFD code is used to conduct the numerical simulation. The 3D Reynolds Averaged Navier-Stokes (RANS) equations with one-equation Spalart-Allmaras [14] turbulence model is used. A 3rd order WENO scheme for the inviscid flux [15, 16, 17, 18, 19, 20] and a 2nd order central differencing for the viscous terms [15, 19] are employed to discretize the Navier-Stokes equations. The low diffusion E-CUSP scheme used as the approximate Riemann solver suggested by Zha et al [16] is utilized with the WENO scheme to evaluate the inviscid fluxes. Implicit time marching method using Gauss-Seidel line relaxation is used to achieve a fast convergence rate [21]. Parallel computing is implemented to save wall clock simulation time [22].

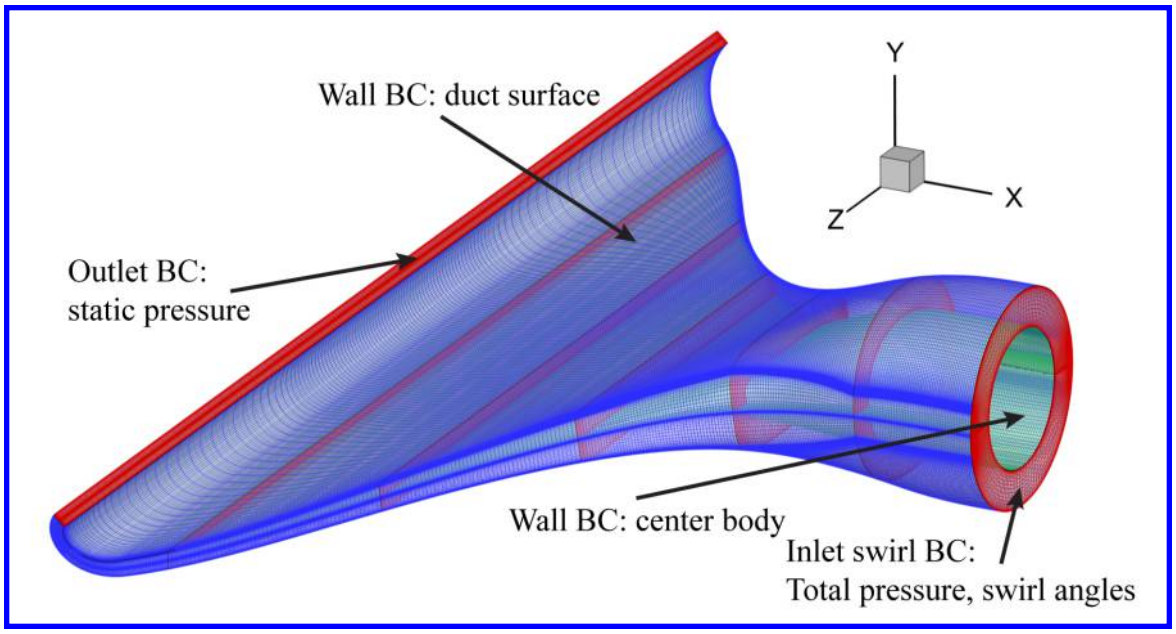

Figure 3: Computational mesh of injection duct in cruise condition.

The 3rd order accuracy no slip condition is enforced on the solid surface with the wall treatment suggested in [23] to achieve the flux conservation on the wall. As shown in Fig. 3, total pressure, total temperature and flow angles are specified at the duct inlet as boundary conditions. Static pressure is specified at the duct outlets as boundary conditions. The specific boundary conditions are based on the design of 2D CFJ airfoils [13] and micro-compressors [24]. The cross section faces of the ducts are meshed using "H" topology. Three hundreds points are placed in the streamwise direction, 60 points and 180 points are placed in the radial and circumferential direction. The total mesh size is 3.24 millions points, split into 12 blocks for the parallel computation. The first grid point on the duct surface is placed at $y^+ \approx 1$.

3 Results

There are total three ducts are designed in this work: (1) the suction duct (SD); (2) the injection duct (ID); (3) the injection duct with guiding vanes (ID-GV). For the injection duct, we also need to consider the center body (CB) geometry. The predetermined inlet and outlet dimensions are listed in Table 1. We can see in Table 1 that the SD is actually a converging duct, which will have favorable pressure gradient. The ID has the same A_{cs} at the inlet and outlet, which is more prone to flow separation.

Table 1: Predetermined inlet and outlet parameters of the injection and suction ducts

Designs	a^{in}	b^{in}	η^{in}	A^{in}_{sc}	a^{out}	b^{out}	η^{out}	A^{out}_{sc}
SD	21	0.48	100	40.33	3.24	3.24	2	33
ID	3.24	3.24	2	33	21	0.23	100	19.62
CB	2.06	2.06	2	13.32	N/A	N/A	N/A	N/A

3.1 Suction Duct Design

Fig. 4 (a) shows the geometry of the suction duct, and Fig. 4 (b) shows the profile of the superellipse cross section area A_{cs} along the duct meanline. The simulation results show that the A_{cs} is the most important parameter that affects the performance of the duct. In addition, the supperellipse semi major axis a profile is also critical in the suction duct design, especially at the start and the end of the duct.

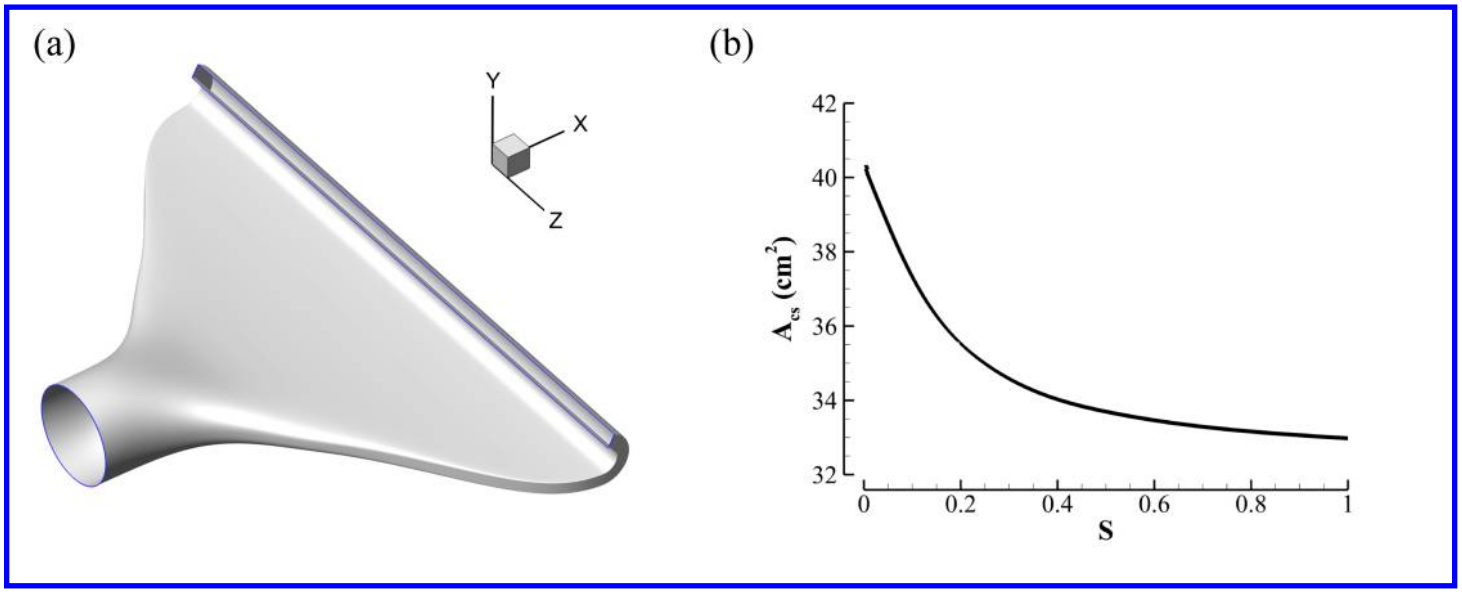

Figure 4: (a) Geometry of the suction duct; (b) the profile of the superellipse cross section area. The x-coordinate shows the cross section face locations from the duct inlet to outlet (0 to 1).

Fig. 5 shows the 2D flow slices along z-direction (colored by Mach number) and the corresponding streamlines for the SD case. We can see in Fig. 5 (a) that the flow is much stronger near the bottom part of the suction duct, which is due to the duct turning near the duct inlet. The centrifugal force push the flow to the bottom part of the duct. In contrast, the flow at the top part of the duct is weak and easy to separate. In order to prevent the flow separation, the A_{cs} is tuned to be converging faster in the duct turning part (Fig. 4 b). Fig. 5 (b) shows three slices with streamlines on them, and no flow separation can be observed.

Fig. 6 (a) shows the 2D flow slices along stream wise direction (colored by total pressure). As expected, the total pressure is stronger near the bottom part of the duct, and it keep decreasing along the duct. Fig. 6 (b) shows the mass flow averaged total pressure distribution along the stream wise direction. We can see that the total pressure linearly decreases along the duct and the total pressure recovery is 99% in this case.

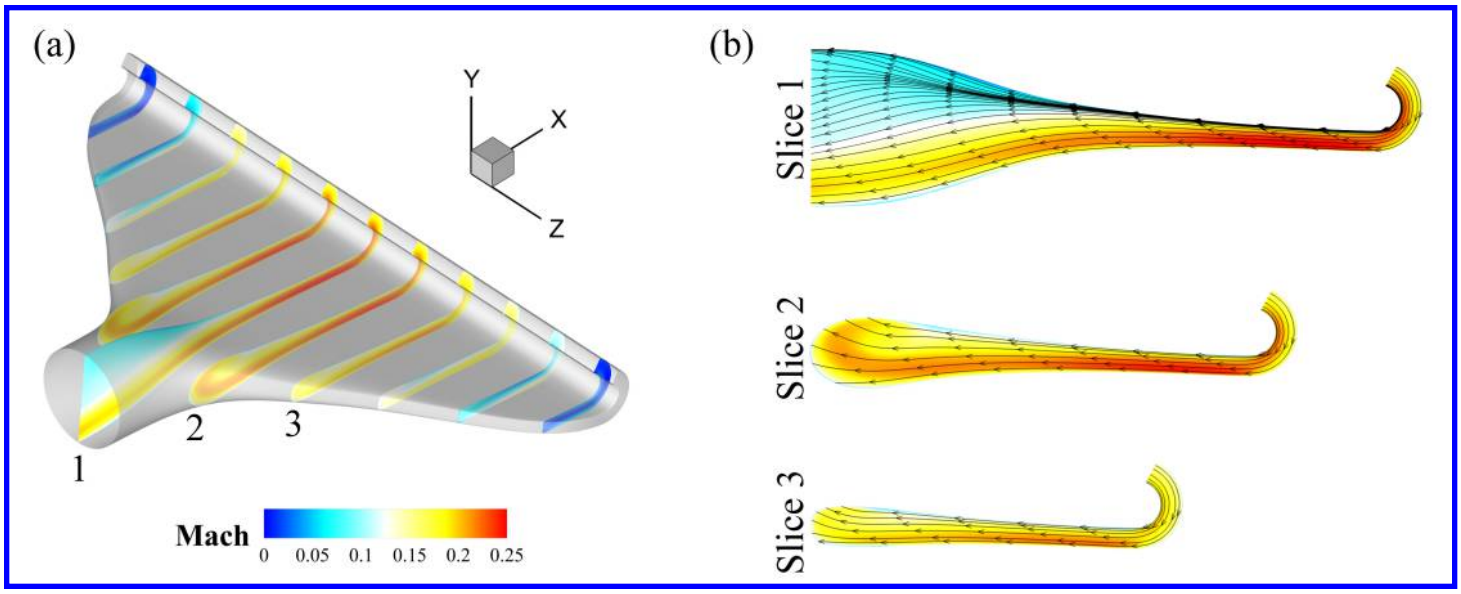

Figure 5: (a) 2D flow slices along the z-direction of the suction duct, colored by Mach number; (b) streamlines on slice 1, 2, and 3.

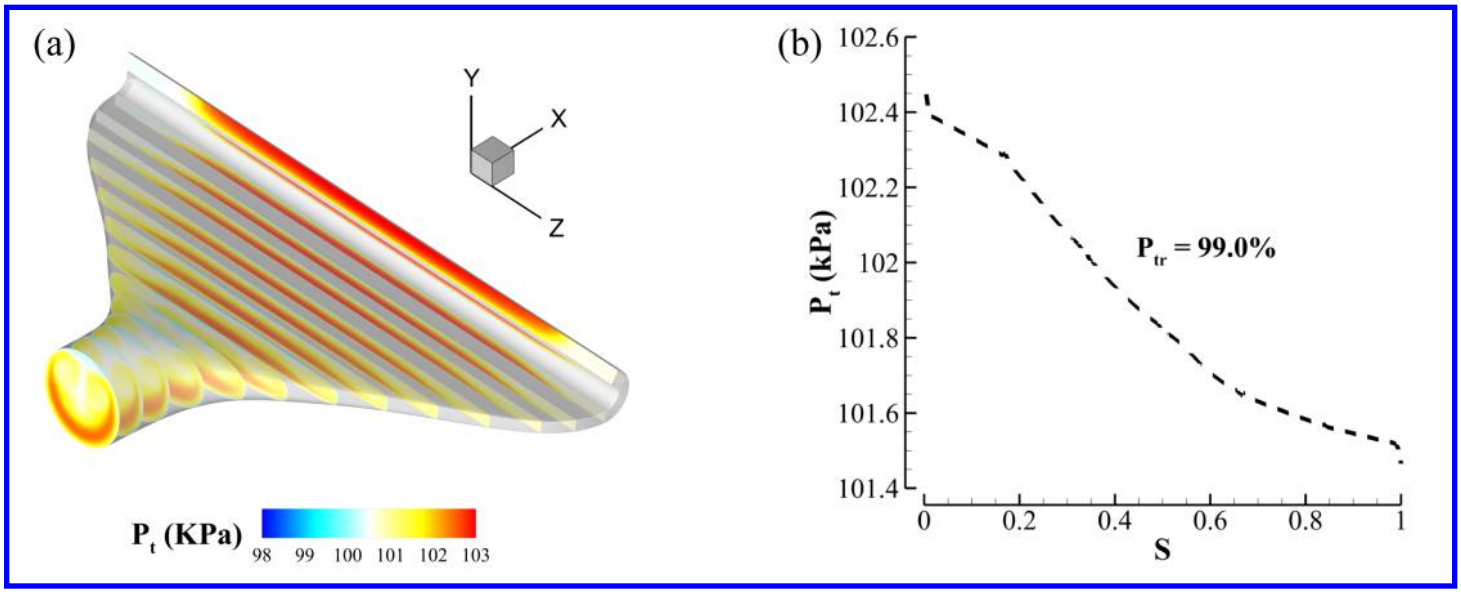

Figure 6: (a) 2D flow slices along the stream wise direction of the suction duct, colored by total pressure; (b) mass flow averaged total pressure distribution along the stream wise direction of the suction duct.

3.2 Injection Duct Design

Fig. 7 (a) shows the geometry of the injection duct, and Fig. 7 (b) shows the profile of the superellipse cross section area. Different from the suction duct, the injection duct have a center body to guide the swirl flow directly coming out of the micro-compressor to prevent flow separation. The simulation results show that the a distribution of the center body is the key to prevent flow separation near the surface of the center body. In addition, the A_{cs} is tuned to decrease near the inlet and stay unchanged at the rest part of the duct. It will also help to improve

the attachment of the flow. The η of the injection duct and the center body share the same profile as shown in Fig. 7 (b).

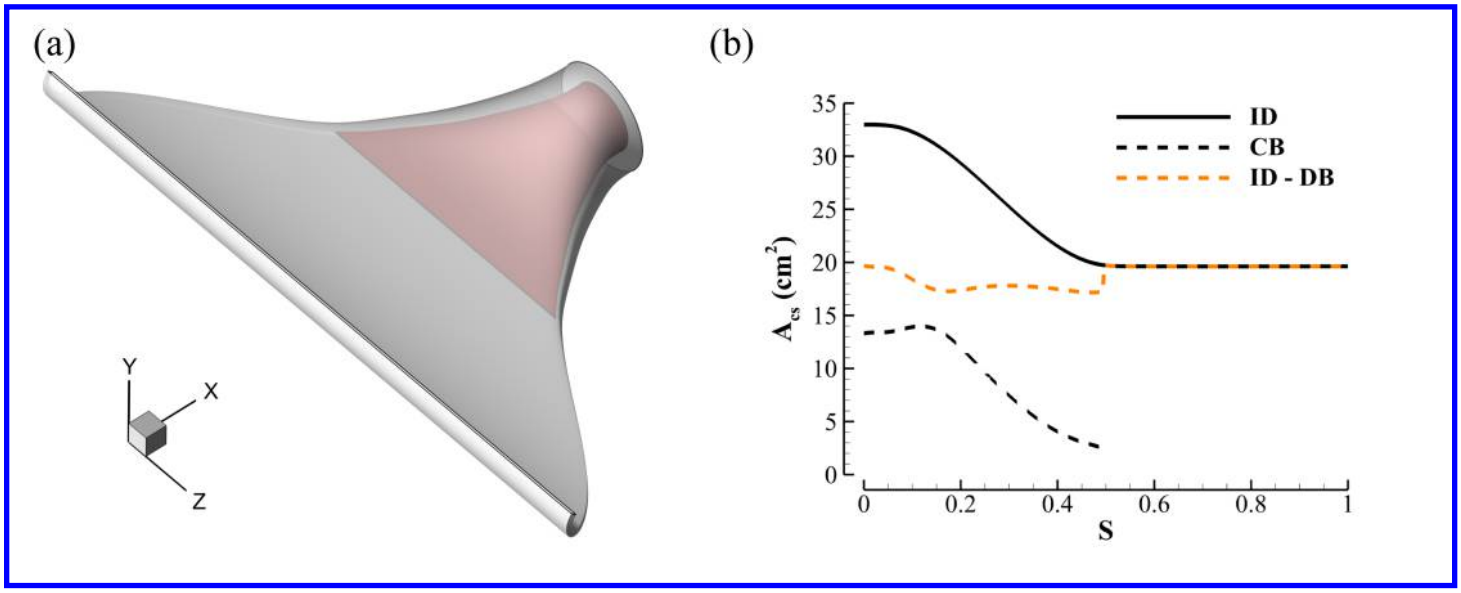

Figure 7: (a) Geometry of the injection duct; (b) the profile of the superellipse cross section area. The x-coordinate shows the cross section face locations from the duct inlet to outlet (0 to 1).

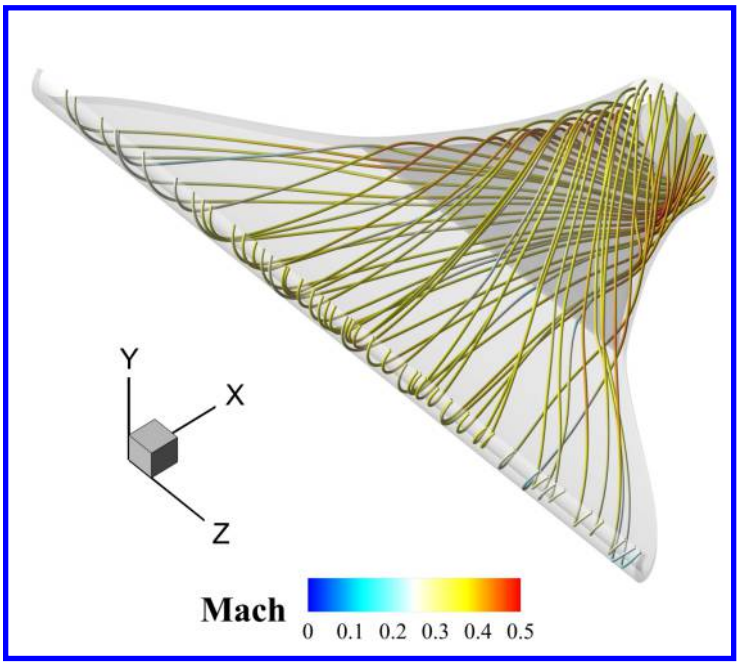

Figure 8: Simulated 3D streamlines inside the injection duct. Colored by Mach number.

We first look at the 3D streamlines (colored by Mach number) of the this case. The results is plotted in Fig. 8. We can see that there is a strong swirl flow directly coming out of the micro-compressor of this case. The flow at the two sides of the center body is stronger and at the top and bottom surface of the center body is weaker. The center body guide the flow well and the flow is very healthy through out the duct.

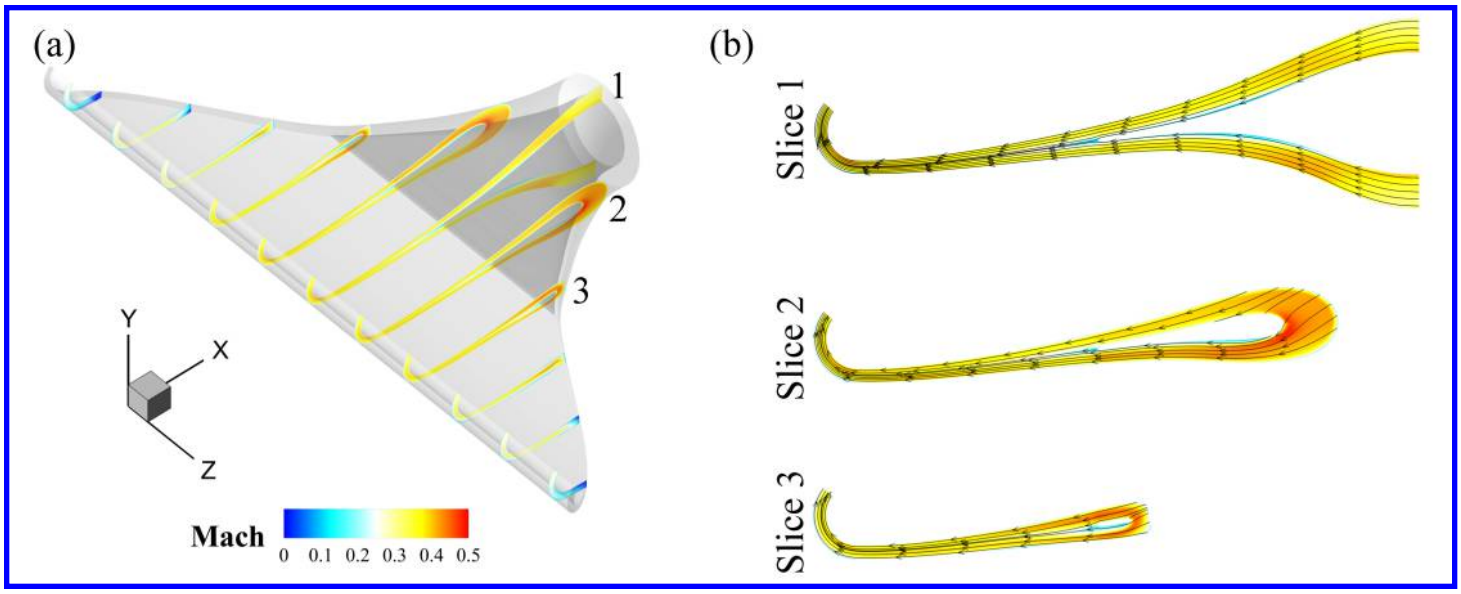

Figure 9: (a) 2D flow slices along the z-direction of the injection duct, colored by Mach number; (b) streamlines on slice 1, 2, and 3.

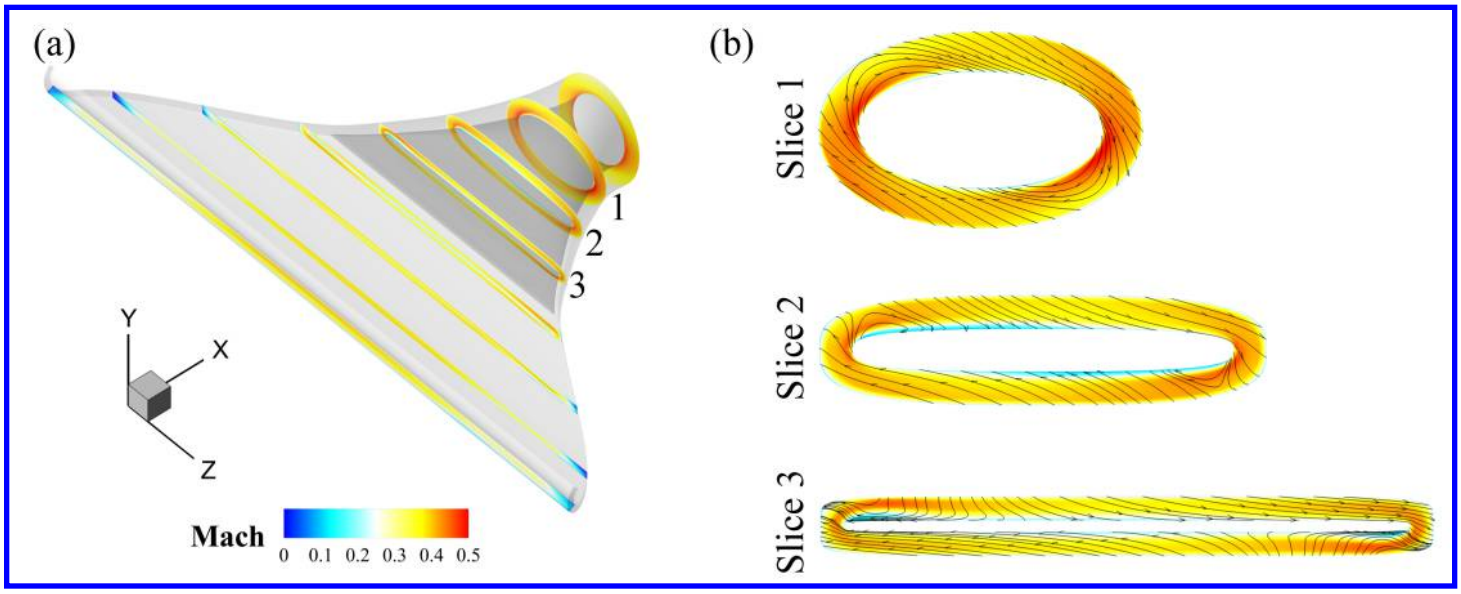

Figure 10: (a) 2D flow slices along the span wise direction of the injection duct, colored by Mach number; (b) streamlines on slice 1, 2, and 3.

Fig. 9 and Fig. 10 show the 2D flow slices along z-direction and stream wise direction, respectively (colored by Mach number). The corresponding streamlines are also plotted on the slices for the ID case. We can see in Fig. 9 (a) and Fig. 10 (a) that the flow is stronger near the two sides of the center body, which is due to the acceleration of the swirl flow when it's passing though the thin edge of the center body. That's why the center body a profile is crucial, and any improper profiles will lead to large flow separation around the edges of the center body. Fig. 9 (b) and Fig. 10 (b) show six slices along z-direction and stream wise direction with streamlines on them, and no flow separation can be observed in both directions here.

Fig. 11 (a) shows the 2D flow slices along stream wise direction (colored by total pressure). As expected, the total pressure keeps decreasing along the duct. Fig. 11 (b) shows the mass flow averaged total pressure distribution along the stream wise direction. We can see that the total pressure linearly decreases along the duct with a faster rate comparing to that in the suction duct case (Fig. 6 b), since the large swirl angle of the flow and the center body increase the energy loss inside the injection duct. However, the total pressure recovery is still acceptable (95%).

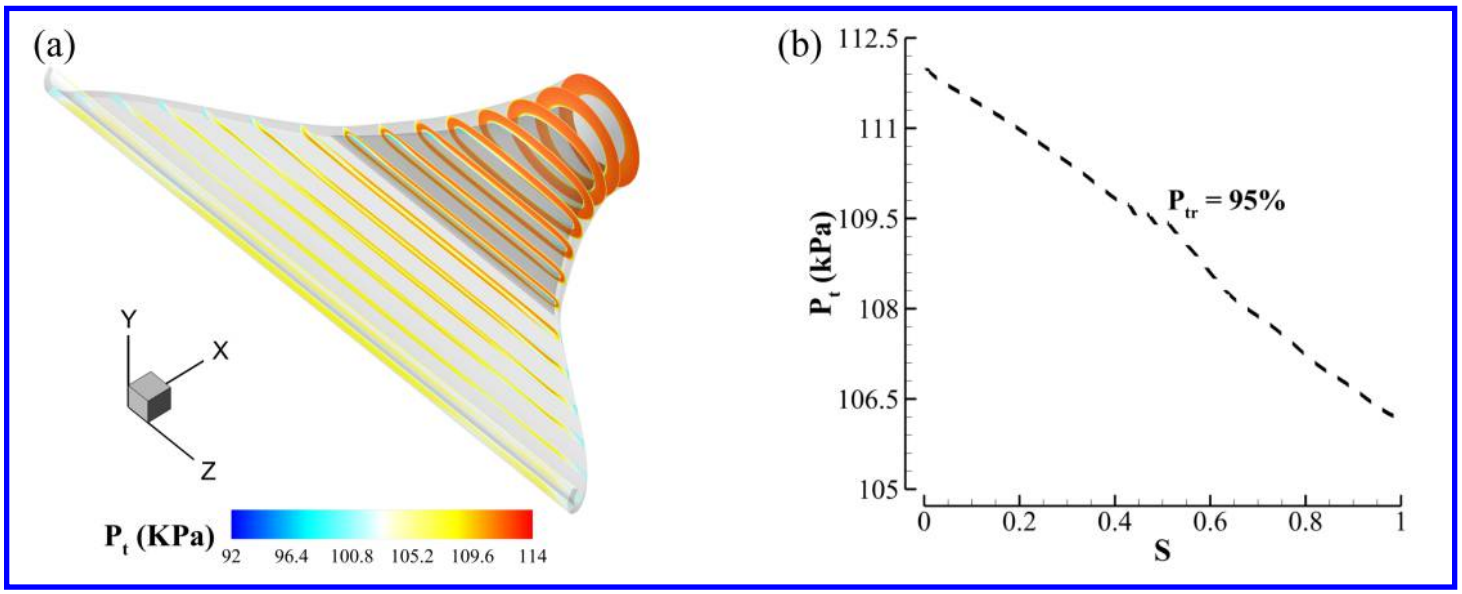

Figure 11: (a) 2D flow slices along the stream wise direction of the injection duct, colored by total pressure; (b) the corresponding mass flow averaged total pressure distribution along the stream wise direction.

3.3 Injection Duct with Guiding Vanes

A nice and uniformly distributed mass flow at the injection duct outlet is very important to the overall CFJ airfoil performance [25]. However, due to the large width difference between the duct inlet and outlet, the flow deviation angle β ($\beta = atan(w/\sqrt{u^2+v^2})$) is large near the outlet of the injection duct as shown in the 3D streamlines plot (Fig. 8). In order to reduce the β angle and to obtain a more favorable mass flow distribution at the injection duct outlet, guiding vanes are added just down stream of the center body to redirect the flow.

Fig. 12 (a) shows the vane geometries inside the injection duct. The vanes have zero thickness and are configured based on the simulation results shown in section 3.2, which ensures that the vane incident angles are zero. The vanes are bent and twisted to guide the flow to the main stream direction (minimize w velocity down stream of the vanes). Fig. 12 (b) shows the simulated 3D streamlines (colored by Mach number) of the this case. We can see that the vanes nicely guide the flow down stream of the center body.

We further measure the average β angle distribution in span wise direction at the duct outlets for the cases with and without guiding vanes. The results are plotted in Fig. 13 (a). We can see that the β angle is significantly decreased with the vanes (about 50%). As a result, the mass flow distribution at the duct outlet is more favorable, especially near the two ends of the outlet (Fig. 13 b).

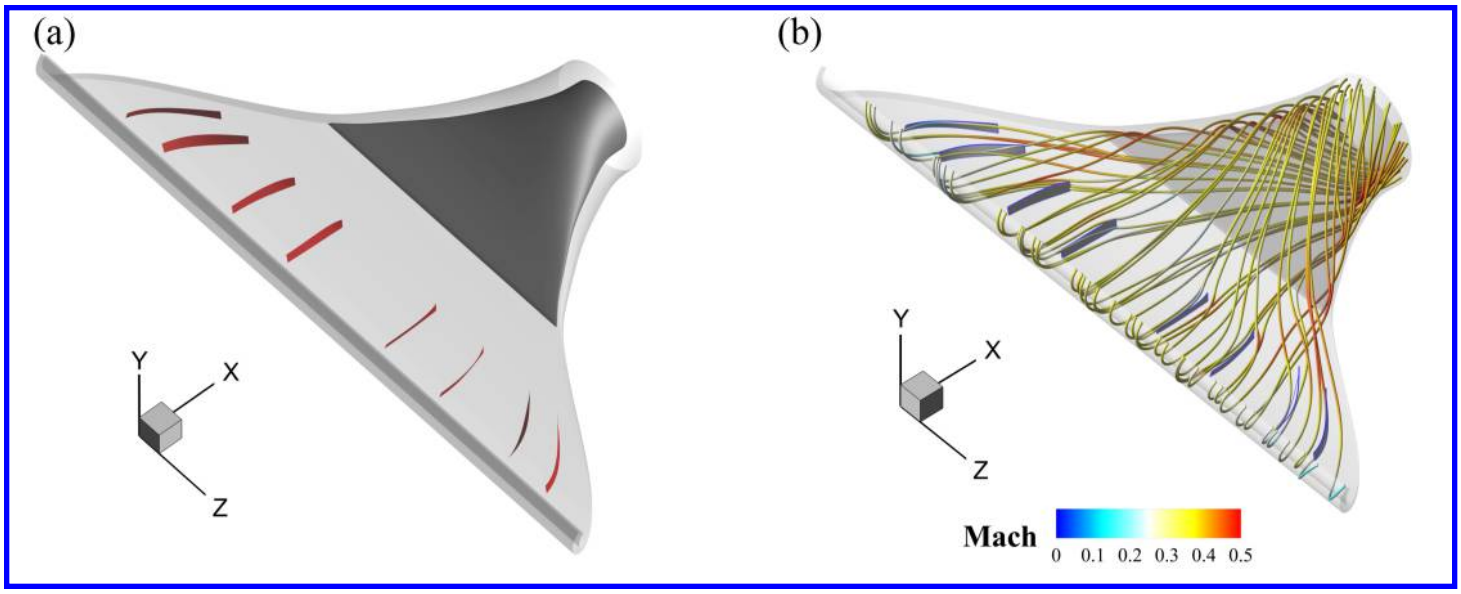

Figure 12: (a) Guiding vane geometries inside the injection duct; (b) simulated 3D streamlines inside the injection duct with guiding vanes. Colored by Mach number.

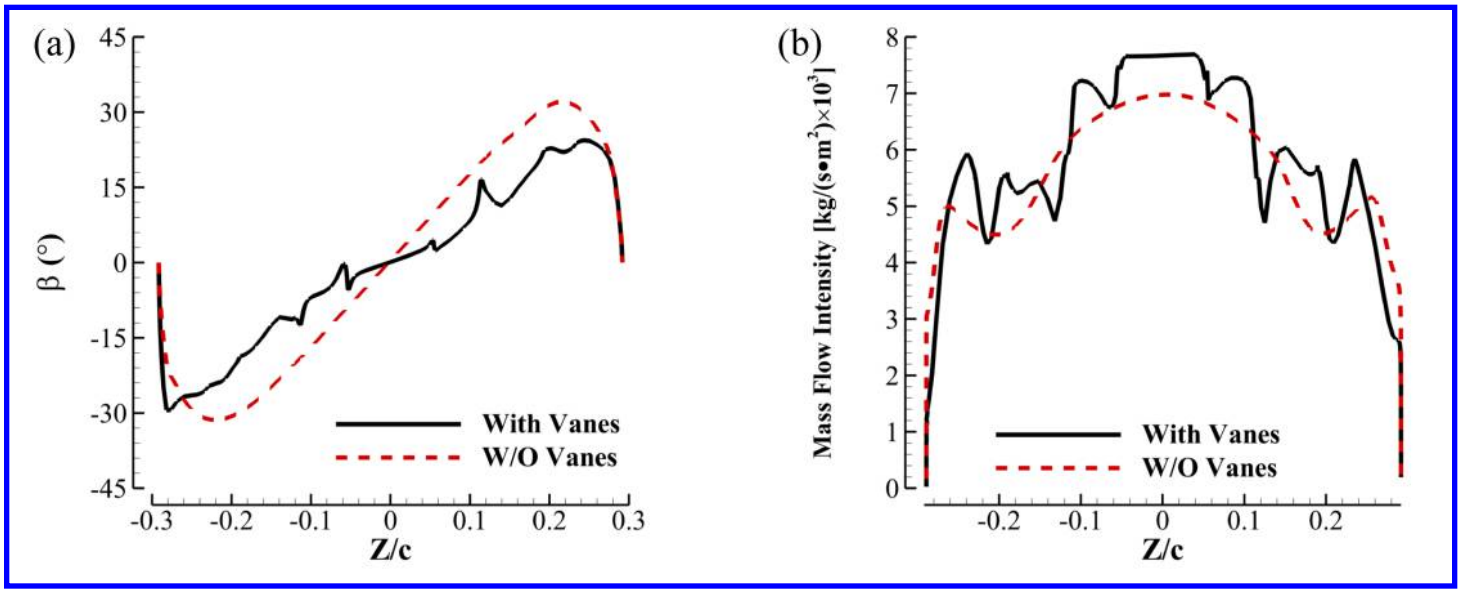

Figure 13: (a) Average β angle distribution in span wise direction at the injection duct outlet for the cases with and without guiding vanes; (b) mass flow intensity distribution in span wise direction at the injection duct outlet for the cases with and without guiding vanes.

Fig. 14 (a) shows the 2D flow slices along the stream wise direction (colored by total pressure) of the case with guiding vanes. We can see from the figure that the total pressure around the vanes decreases a little bit by introducing more walls inside the duct. Fig. 14 (b) shows the mass flow averaged total pressure distribution along the stream wise direction. The total pressure still linearly decreases along the duct, and the total pressure recovery decreased to 93.7%. Overall, a more favorable mass flow distribution at the injection duct outlet is obtained at the cost of the duct efficiency.

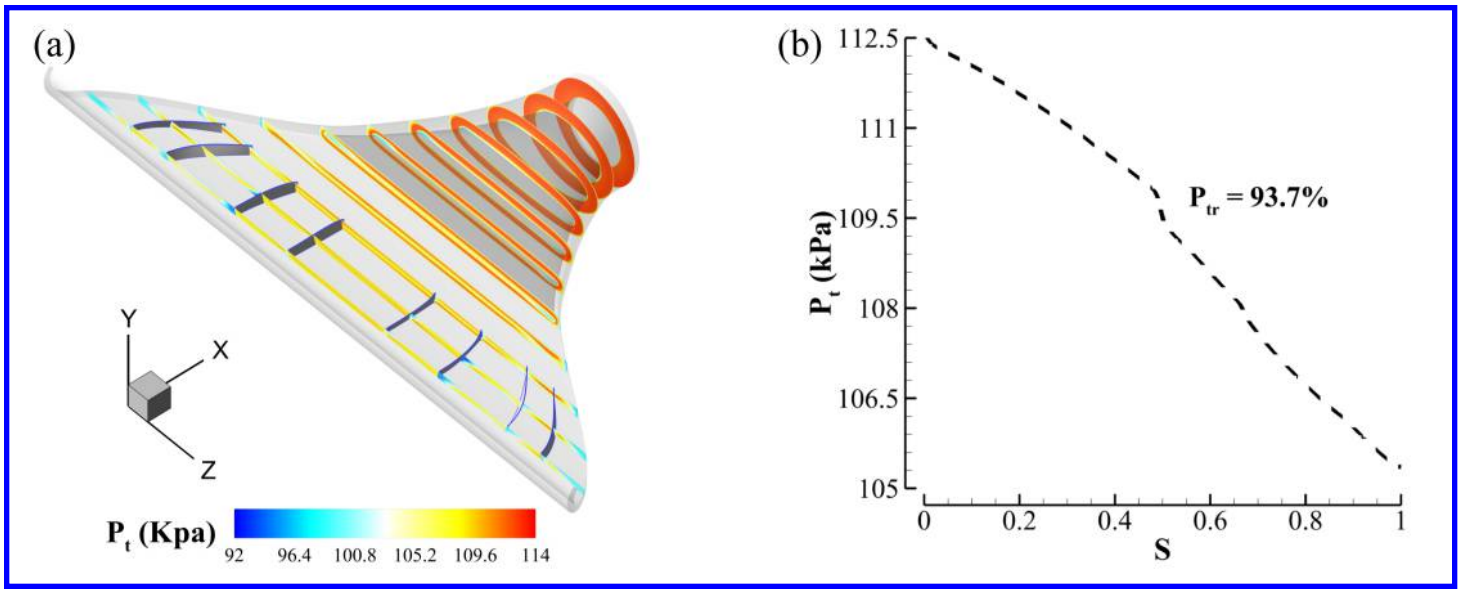

Figure 14: (a) 2D flow slices along the stream wise direction of the injection duct with guiding vanes, colored by total pressure; (b) the corresponding mass flow averaged total pressure distribution along the stream wise direction.

4 Conclusions

In this work, we present the designs of injection and suction ducts of co-flow jet (CFJ) flow control airfoils with embedded micro-compressor actuator in cruise condition. The simulation results show that the superellipse semi major axis is important to improve the total pressure recovery for the suction duct. The center body a profile is critical in the injection duct design due to the large flow swirl angle at the duct inlet. Moreover, the injection duct guiding vanes can provide a more uniformly distributed mass flow at the duct outlet. Our optimized suction duct presents 99% total pressure recovery. The optimized injection duct shows 95% total pressure recovery without guiding vanes, and shows 93.7% total pressure recovery with guiding vanes.

5 Acknowledgment

This project is sponsored by the Defense Advanced Research Projects Agency and monitored by the program manager Jean-Charles Ledé under Cooperative Agreement No.: HR0011-16-2-0052. The content of the information does not necessarily reflect the position or the policy of the Government, and no official endorsement should be inferred. The simulations are conducted on Pegasus supercomputing system at the Center for Computational Sciences at the University of Miami.

References

[1] G.-C. Zha and D. C. Paxton, "A Novel Flow Control Method for Airfoil Performance Enhancement Using Co-Flow Jet." *Applications of Circulation Control Technologies*, Chapter 10, p. 293-314, Vol. 214, Progress in Astronautics and Aeronautics, AIAA Book Series, Editors: Joslin, R. D. and Jones, G.S., 2006.

[2] G.-C. Zha, W. Gao, and C. Paxton, "Jet Effects on Co-Flow Jet Airfoil Performance," *AIAA Journal, No. 6,*, vol. 45, pp. 1222–1231, 2007.

[3] G.-C. Zha, C. Paxton, A. Conley, A. Wells, and B. Carroll, "Effect of Injection Slot Size on High Performance Co-Flow Jet Airfoil," *AIAA Journal of Aircraft*, vol. 43, 2006.

[4] G.-C. Zha, B. Carroll, C. Paxton, A. Conley, and A. Wells, "High Performance Airfoil with Co-Flow Jet Flow Control," *AIAA Journal*, vol. 45, 2007.

[5] Wang, B.-Y. and Haddoukessouni, B. and Levy, J. and Zha, G.-C., "Numerical Investigations of Injection Slot Size Effect on the Performance of Co-Flow Jet Airfoil," *Journal of Aircraft*, vol. Vol. 45, No. 6,, pp. pp.2084–2091, 2008.

[6] B. P. E. Dano, D. Kirk, and G.-C. Zha, "Experimental Investigation of Jet Mixing Mechanism of Co- Flow Jet Airfoil." AIAA-2010-4421, 5th AIAA Flow Control Conference, Chicago, IL, 28 Jun - 1 Jul 2010.

[7] B. P. E. Dano, G.-C. Zha, and M. Castillo, "Experimental Study of Co-Flow Jet Airfoil Performance Enhancement Using Micro Discreet Jets." AIAA Paper 2011-0941, 49th AIAA Aerospace Sciences Meeting, Orlando, FL, 4-7 January 2011.

[8] A. Lefebvre, B. Dano, W. Bartow, M. Fronzo, and G. Zha, "Performance and energy expenditure of coflow jet airfoil with variation of mach number," *Journal of Aircraft*, vol. 53, no. 6, pp. 1757–1767, 2016.

[9] A. Lefebvre, G-C. Zha, "Numerical Simulation of Pitching Airfoil Performance Enhancement Using Co-Flow Jet Flow Control," *AIAA paper 2013-2517*, June 2013.

[10] A. Lefebvre, G-C. Zha, "Cow-Flow Jet Airfoil Trade Study Part I : Energy Consumption and Aerodynamic Performance," *32nd AIAA Applied Aerodynamics Conference, AIAA AVIATION Forum, AIAA 2014-2682*, June 2014.

[11] A. Lefebvre, G-C. Zha, "Cow-Flow Jet Airfoil Trade Study Part II : Moment and Drag," *32nd AIAA Applied Aerodynamics Conference, AIAA AVIATION Forum, AIAA 2014-2683*, June 2014.

[12] J. R. Burley II, L. S. Bangert, and J. R. Carlson, "Static investigation of circular-to-rectangular transition ducts for high-aspect-ratio nonaxisymmetric nozzles." NASA Technical Paper 2534, 1986.

[13] Yang, Yunchao and Zha, Gecheng, "Super-Lift Coefficient of Active Flow Control Airfoil: What is the Limit?," *AIAA Paper 2017-1693, AIAA SCITECH2017, 55th AIAA Aerospace Science Meeting, Grapevine, Texas*, p. 1693, 9-13 January 2017.

[14] P. R. Spalart and S. R. Allmaras, "A one-equation turbulence model for aerodynamic flows," in *30th Aerospace Sciences Meeting and Exhibit, Aerospace Sciences Meetings, Reno, NV, USA, AIAA Paper 92-0439*, 1992.

[15] Y.-Q. Shen and G.-C. Zha, "Large Eddy Simulation Using a New Set of Sixth Order Schemes for Compressible Viscous Terms ," *Journal of Computational Physics*, vol. 229, pp. 8296–8312, 2010.

[16] Zha, G.C., Shen, Y.Q. and Wang, B.Y., "An improved low diffusion E-CUSP upwind scheme ," *Journal of Computer and Fluids*, vol. 48, pp. 214–220, Sep. 2011.

[17] Y.-Q. Shen and G.-Z. Zha , "Generalized finite compact difference scheme for shock/complex flowfield interaction," *Journal of Computational Physics*, vol. doi:10.1016/j.jcp.2011.01.039, 2011.

[18] Shen, Y.-Q. and Zha, G.-C. and Wang, B.-Y., " Improvement of Stability and Accuracy of Implicit WENO Scheme," *AIAA Journal*, vol. 47, No. 2, pp. 331–344, 2009.

[19] Shen, Y.-Q. and Zha, G.-C. and Chen, X.-Y., " High Order Conservative Differencing for Viscous Terms and the Application to Vortex-Induced Vibration Flows," *Journal of Computational Physics*, vol. 228(2), pp. 8283–8300, 2009.

[20] Shen, Y.-Q. and Zha, G.-C. , " Improvement of the WENO Scheme Smoothness Estimator," *International Journal for Numerical Methods in Fluids*, vol. DOI:10.1002/fld.2186, 2009.

[21] G.-C. Zha and E. Bilgen, "Numerical Study of Three-Dimensional Transonic Flows Using Unfactored Upwind-Relaxation Sweeping Algorithm," *Journal of Computational Physics*, vol. 125, pp. 425–433, 1996.

[22] B.-Y. Wang and G.-C. Zha, "A General Sub-Domain Boundary Mapping Procedure For Structured Grid CFD Parallel Computation," *AIAA Journal of Aerospace Computing, Information, and Communication*, vol. 5, No.11, pp. 2084–2091, 2008.

[23] Y.-Q. Shen, G.-C. Zha, and B.-Y. Wang, "Improvement of Stability and Accuracy of Implicit WENO Scheme ," *AIAA Journal*, vol. 47, pp. 331–344, 2009.

[24] PCA engineers, "Design of a mixed flow fan." Internal Report to University of Miami, 2017.

[25] Y. Ren and G. Zha, "Simulation of 3d co-flow jet airfoil with embedded micro-compressor actuator," in *2018 AIAA Aerospace Sciences Meeting, AIAA 2018-0330*, p. 0330, 2018.